

# Measurement of Small Electron Beam Spots \*

PETER TENENBAUM

*Stanford Linear Accelerator Center, Stanford University, Stanford, California, USA*

TSUMORU SHINTAKE

*High Energy Accelerator Research Organization, Tsukuba, Japan*

## Abstract

Measurements of transverse beam size are tremendously important to the performance of  $e^+e^-$ -linear colliders. In this paper we review the traditional technologies used to make such measurements, such as profile monitors and wire scanners, and the limitations on same. We then introduce a new tool for electron beam size measurement: Compton-scattered laser light, which may be used as an unbreakable “wire” or in the form of an interferometer beam size monitor. We describe the use of such an interferometer BSM, noting both the general issues related to its design and operation and the specific experiences with such an interferometer at the Final Focus Test Beam (FFTB) at SLAC. We conclude by considering the ultimate limits of the laser-interferometer BSM.

Submitted to *Annual Review of Nuclear and Particle Science*.

---

\*Work supported by the Department of Energy, Contract DE-AC03-76SF00515.

# 1 INTRODUCTION

Transverse beam size measurements are now an essential diagnostic for high-performance linear accelerators, such as  $e^+e^-$  linear colliders and linac-pumped FELs. Beam size diagnostics are used both for initial tuning of the beam line and for control of slow instabilities which dilute the tuned performance over time. The Stanford Linear Collider (SLC) measures the beam size at over 50 locations in the linac and beam delivery areas [1]; the Final Focus Test Beam (FFTB) at SLAC measures the beam size at 7 locations downstream of the SLAC linac [2], and future linear collider designs envision as many as 100 such measurements.

The uses of beam size measurement can be divided into four general categories, which are described below.

## 1.1 Emittance

Linear accelerators typically consist of RF accelerating structures interleaved with quadrupole magnets which focus the beam. Misaligned structures or quadrupoles can cause an increase in the beam size: the former through wakefields (electric fields from the beam head deflecting the tail), the latter through dispersion (unequal deflection of particles of different energies by the magnetic field of the quadrupole). Either of these effects results in an increase in the incompressible phase volume of the beam in  $(x, x')$  or  $(y, y')$  phase space. In addition, many facilities such as linear colliders rely on the acceleration of flat beams, in which one plane has a much smaller phase volume than the other. In such environments, cross-plane coupling from rolled quadrupole magnets can cause the smaller of the two phase volumes to be enlarged.

The deleterious effects of wakefields and dispersion are measured by fully reconstructing the size and shape of the beam's phase space in  $x$  or  $y$ . The phase space typically takes the form of an ellipse in the  $(x, x')$  or  $(y, y')$  plane [3]; thus the phase space can be characterized by 3 independent parameters. The two parameterizations usually used are the independent second moments of the beam distribution ( $\langle x^2 \rangle$ ,  $\langle x'^2 \rangle$ , and  $\langle xx' \rangle$ ) or the emittance and Twiss parameters ( $\epsilon$ ,  $\beta$ ,  $\alpha$ ) [4]. While the two

parameterizations are equivalent and each is easily translated to the other, the Twiss parameterization has the advantage of explicitly separating the incompressible phase volume, the emittance, from the parameters related to the orientation and aspect ratio of the ellipse.

The reconstruction of the beam ellipse in phase space requires measurement of three second moments of the beam at a given point in the accelerator, while beam size measurement devices can only realistically measure the  $\langle x^2 \rangle$  moment at a point. Full emittance measurements require measuring the beam size at different betatron phase advances, and using knowledge of the beam transport properties to reconstruct the second moments at a given point. the most common technique for this is to use a single beam size monitor and change the strength of an upstream quadrupole; this changes the phase advance between the quad's upstream face and the monitor [5]. A less invasive technique is to use several monitors at different locations, and make a single measurement on each monitor; this permits reconstruction of the phase ellipse without changing the any beamline magnet [6]. This is the preferred technique for modern high-performance linacs.

## 1.2 Energy Spread

Errors in klystron timing and phasing with respect to the beam can result in reduced energy gain and increased energy spread, which is usually unacceptable to any experiment to which beam from a linac is delivered (especially final focus systems of linear colliders and linac-driven FELs). The beam energy spread is measured by generating a strong correlation between transverse position and beam energy at a location in the beamline, and measuring the transverse beam size. If the correlation (denoted by  $\eta$  or  $D$  and known as dispersion) is known and is large enough that the dispersive beam size dominates the monochromatic beam size at the location, then the energy spread (and often details of the spectrum) can be calculated directly. Since it is often not convenient to provide such a location, typically some knowledge of the beam's monochromatic size at the monitor's location is needed to deconvolve the latter.

### 1.3 Interaction Point Parameters

The interaction point (IP) of a linear collider typically requires an extremely small spot size to provide adequate luminosity for the experiment. The Stanford Linear Collider (SLC) reduces beams to RMS sizes of 2 microns (horizontal) by 0.4 microns (vertical) [7]. Future linear colliders may have spot sizes as small as 0.2 microns by 2.8 nanometers [8]. Because the final focus systems for such colliders usually have strong aberrations which must be carefully corrected, direct measurement of the focused spot size is crucial to linear collider performance.

A related measurement is the beam angular divergence at the interaction point. This is determined by measuring the beam size at a point some distance from the interaction point, where the spot size is dominated by the IP divergence. The divergence measurement has two uses. The first is background control: unacceptably large divergences result in beam particles scattering into the experimental detectors, which must be prevented to preserve data quality. The second is betatron matching: while the IP beam size can be dominated by aberrations, the IP angular divergence is determined by linear beam optics; by knowing the divergence,  $\theta^*$ , and the beam emittance, the betatron function at the IP,  $\beta^*$ , can be computed directly:  $\theta^* = \sqrt{\epsilon/\beta^*}$ . This allows unambiguous determination of whether an overlarge IP beam size is due to a linear optics mismatch or aberrations.

### 1.4 Non-Gaussian Tails

In addition to measuring the RMS transverse size of a beam, many beam size monitors can measure higher-moment information about the beam distribution. The most useful of these is the third moment, the asymmetry of the beam profile. Wakefields which deflect the downstream end of a bunch often result in profiles with a strong asymmetry, as shown in Figure 1. While wakefield tails can be tuned by measuring the emittance, it is often more efficient to use a single beam size monitor with a severely asymmetric beam as the diagnostic signal for wakefield tuning strategies.

## 2 CONVENTIONAL BEAM SIZE MONITORS

Because beam size measurements are so widely used, several different techniques have been developed for performing the measurements. We describe some of the most widely applicable below.

### 2.1 Profile Monitors

A general schematic of a beam profile monitor is shown in Figure 2: an intercepting screen is inserted into the beam path at an angle of  $45^\circ$ ; the emitted light is imaged onto a camera, and can thus be transported to a video display or digitizer. In order to ensure that the screen emits light, phosphorescent coatings are usually employed [9]; more recent profile monitors utilize optical transition radiation [10] or emission from YAG crystals [11].

Profile monitors are almost always the easiest beam size measurement devices to employ. Consequently, even high-performance linacs often have several profile monitors for use as the “diagnostic of last resort.” A full horizontal/vertical profile can be produced by a single beam pulse, all details of the distribution in  $x$  and  $y$  of the charge are preserved, and generally the image can be transmitted to a video screen (if not a digitizer) on every pulse, allowing real-time evolution of the beam to be observed.

Profile monitors suffer from several disadvantages as well. Most obviously, they are invasive: the amount of beam which is scattered out of the accelerator is large, and it is almost never possible to recapture and deliver a bunch which has passed through a profile monitor. Consequently beam diagnostics which rely on profile monitors compete with delivery of beams to experimental areas, and also cause irradiation of the surrounding equipment (including the profile monitor’s camera, a frequent cause of camera failure). Profile monitors are limited in their spatial resolution: phosphorescent screens are limited by the phosphor grain size to a typical resolution of  $20\text{ }\mu\text{m}$  [12], while other profile monitors are limited by the optics of the light transport to the camera or the pixel size of the digitizer. Many profile monitors are

limited in their temporal resolution by persistence of the light emitted, especially phosphorescent screens. Finally, profile monitors are often limited in their dynamic range: a camera arrangement which produces a good image when the beam is small often is too diffuse to be digitized when the beam is large; conversely, if the profile monitor is set up properly for large beams the image saturates for small ones.

One arrangement of profile monitors which reduces invasiveness is shown in Figure 3: the profile monitors are off-axis from the accelerator, and a pulsed kicker deflects the beam onto the screens. A set of 8 such screens is installed at the end of the SLAC linac; one electron pulse and one positron pulse is “stolen” for the screens by the kickers every 8 seconds (1 pulse out of 960, resulting in a 0.1% luminosity reduction). The images from the screens are digitized and transmitted to the control room, resulting in a near-real-time display of the beam profile at the end of the linac [13].

## 2.2 Wire Scanners

Wire scanners, sometimes known as “flying wires,” are in common use at storage rings [14] and at linear accelerators [15]. A general schematic is shown in Figure 4: a yoke with one or more fibers (ranging in diameter from a few millimeters to a few microns) is attached to a translation stage which is capable of moving the wire across the path of the beam. The intersection of the beam and the wire produces a shower of bremsstrahlung photons and degraded electrons, whose intensity is proportional to the amount of beam intercepted by the wire. If a detector is placed at an appropriate place, the resulting detector intensity versus position looks like Figure 1, and the beam size and shape (in one dimension) are directly reconstructed.

Wire scanners are substantially more difficult to use than profile monitors. The scanner is a precision stepped device rather than a simple in/out screen; a detector needs to be placed in an appropriate location (where the signal is present but backgrounds are not unacceptable), provided with high voltage, and timed to the beam’s presence; design of the wire scanner and its detector need to be carefully optimized against the size and intensity of the beam. Furthermore, the wire scanner requires

multiple pulses (or multiple turns in a storage ring) to generate a measurement. Since linear accelerators are typically prone to pulse-to-pulse jitter it is sometimes necessary to measure the beam position on each pulse used in a wire scan and correct for changes in same.

Despite their many difficulties, wire scanners are the measurement tool of choice for most accelerators. One reason is that wire scanners are non-invasive: the actual fraction of the beam which is scattered is small, and therefore wire scanner diagnostics usually do not interfere with beam delivery (although wire scanners close to detectors can produce unacceptable radiation [17]). In addition wire scanners are capable of much higher resolution than profile monitors. One limitation of the beam size resolvable is the diameter of the wire: a wire which is round in cross-section has an RMS size equal to 25% of its diameter [2], which is added in quadrature with the beam size during measurement. Consequently a wire with a  $4\text{ }\mu\text{m}$  diameter is incapable of reliably measuring a beam which has an RMS size smaller than 1 micron; however this is a vast improvement over the capabilities of profile monitors, and wire scanners utilizing 4 micron wires are in common use today [16, 2]. A further limit is the step size of the wire's translation stage: measurement of a  $1\text{ }\mu\text{m}$  RMS beam size requires a stepper which can translate reliably in  $0.3 - 0.5\text{ }\mu\text{m}$  steps.

In principle a higher resolution is always achievable by a smaller wire size, but the realities of materials create an ultimate limit on the achievable wire size. Carbon and tungsten wires with diameters as small as 4 microns have been used; however as the wire diameter is reduced the strength of the wire is also reduced. A  $4\text{ }\mu\text{m}$  carbon wire will be broken by an electron beam at 50 GeV if the ratio of the charge to the beam RMS sizes,  $N/(\sigma_x\sigma_y)$ , exceeds  $500\text{ C m}^{-2}$  (or in more practical terms, if the RMS transverse size for  $3 \times 10^9$  electrons is smaller than  $1\text{ }\mu\text{m}$ ) [17]. Even if smaller wires were achievable, they could not be used for beam size measurements except for bunches very low in charge. While novel techniques to get around this limit are being pursued, for the time being the stress limit described above limits wire scanners to wires  $4\text{ }\mu\text{m}$  in diameter or larger.

## 2.3 Beam-Beam Scans

At the interaction point of a collider, the beams are typically too small and intense to measure with wire scanners and the constraints of the detector rarely allow such scanners. At such location, the beam size is probed by looking at the beam-beam interaction itself.

Two properties of the beam-beam interaction are typically used for interaction point size measurements. The first is the tendency of charged bunches to deflect one another if they collide with an offset. By stepping the position of one beam and measuring the deflection of the other (called a deflection scan), a measurement such as those in Figure 5 is produced. The intensity of the deflection is a function of the bunch charges, the size of the offset, and the beam sizes [18], but in general the slope of the central region of the scan (the region near head-on collisions) is proportional to the convolved transverse sizes of the colliding beams (i.e., the horizontal deflection scales with  $\sigma_{x1}^2 + \sigma_{x2}^2$ ). The second technique is to directly measure the luminosity as a function of the offset between the two beams. In this case one beam position is stepped and the signal from a luminosity monitor is measured, resulting in a measurement such as Figure 6; the RMS width of the plotted figure is equal to the RMS size of the convolved beams. Deflection scans have been used at the SLC [19], PEP-II [20], and LEP [21]; luminosity scans have been used at the SLC [22], PEP-II [20], and HERA [23].

Beam-beam scans do not have the limitations of wire scanners because there is no mechanical wire which can be broken and no apparatus consuming space in the particle physics detector. However, such measurements can only be made in places where the beams collide. Like wire scans, they require multiple bunches or multiple collisions of the same bunch, and often require jitter correction to be accurate. Deflection scans are sensitive to details in the model of the deflection: a mathematical model for round beams will not give correct beam sizes when the beams are quite flat, and disruption (the two beams focusing one another) adds further uncertainty to the model. Furthermore, since beam-beam scans only report the convolved size of the two beams in the collision, they give no insight into which beam is in need of



correction when the result is unacceptably large.

### 3 COMPTON-SCATTERING BEAM SIZE MON-ITORS

A recent development in beam profiling has been the use of lasers to produce an indestructible target for intercepting the beam. This results in a flux of Compton-scattered laser photons propagating downstream in the electron beam's path, and a flux of electrons with degraded energies from the collision which may be deflected by a bending magnet and detected.

#### 3.1 Quantitative Review of Compton Scattering

Extensively detailed studies of Compton scattering from ultra-relativistic electron beams have been published elsewhere (notably [24, 25, 26]). We merely summarize their results as applied to the present problem. Readers are directed to the literature listed above for further details, or to [27], whose general approach we follow.

Consider a laser beam with a power density given by  $\rho_L$  and frequency  $\nu_0$ . The average photon density is given by:

$$\langle n_0 \rangle = \frac{1}{ch\nu_0} \rho_L. \quad (1)$$

The laser collides with an electron beam, of energy  $E$  and relativistic factor  $\gamma$ , with normal incidence; photons from the laser are Compton-scattered into the electron beam's forward direction. If we assume that the laser power is uniformly distributed in  $z$  over a total distance  $D$ , the number of photons which are scattered out of the laser by collision with an electron beam containing  $N_e$  electrons is given by:

$$\langle N_\gamma \rangle = \sigma_C \langle n_0 \rangle D N_e = \frac{\sigma_C}{ch\nu_0} \rho_L D N_e, \quad (2)$$

where  $\sigma_C$  is the Compton scattering cross section. The Compton cross section is related to the Thomson scattering cross-section,  $\sigma_0 \equiv 6.65 \times 10^{-25} \text{cm}^2$ , by the relation:

$$\frac{\sigma_C}{\sigma_0} = \frac{3}{4} \left\{ \frac{1 + \epsilon_1}{\epsilon_1^3} \left[ \frac{2\epsilon_1(1 + \epsilon_1)}{1 + 2\epsilon_1} - \ln(1 + 2\epsilon_1) \right] + \frac{1}{2\epsilon_1} \ln(1 + 2\epsilon_1) - \frac{1 + 3\epsilon_1}{(1 + 2\epsilon_1)^2} \right\}, \quad (3)$$

where  $\epsilon_1 \equiv \frac{\gamma h \nu_0}{m_e c^2}$  is the normalized energy of the laser photons in the electron rest frame. Figure 7 shows the Compton cross-section, as a function of energy, for photons from a Nd:YAG laser ( $\lambda = 1.064 \mu\text{m}$ ) operated on first, second, or fourth harmonics. Note that for the case of head-on collisions between the laser photons and the electron beam, the normalized energy photon energy in the electron rest frame is doubled and the cross-section is reduced.

The energy spectrum of the emerging gamma rays is given by:

$$\frac{d\sigma/\sigma_0}{dw} = \frac{3}{8\epsilon_1} F(\epsilon_1, w), \quad (4)$$

where  $w \equiv h\nu_\gamma/E$  is the energy of the emitted photon normalized to the electron energy, and  $F$  is given by:

$$F(\epsilon_1, w) = \frac{1}{1-w} + 1 - w + \left[ \frac{w}{\epsilon_1(1-w)} \right]^2 - \frac{2w}{\epsilon_1(1-w)}. \quad (5)$$

The maximum photon energy is given by  $h\nu_{\text{max}} = 2E\epsilon_1/(1+2\epsilon_1)$ . Figure 8 shows the spectrum for first, second, and fourth harmonics of Nd:YAG laser photons scattered from 50 GeV and 500 GeV photons.

The critical angle of emitted radiation is given by:

$$\alpha_c = \frac{\sqrt{1+2\epsilon_1}}{\gamma}. \quad (6)$$

The emitted photons will generally be confined within a cone whose half-angle is a few times  $\alpha_c$ .

### 3.2 Example: The SLC/SLD Laser Wire

The most straightforward use of Compton-scattered laser light for beam profiling is the SLC/SLD laser wire [28]. In this case a laser propagating perpendicular to the electron beam is focused to a diffraction-limited waist, and the electron beam is brought into collision with the laser beam at the waist. The electron beam is scanned in position across the laser beam, and the Compton-scattered photons and/or degraded electrons are collected downstream; a plot of detected photons/electrons

versus electron beam position reveals the size of the electron beam. In this case, the laser beam is used as a wire scanner with an unbreakable and extremely narrow wire.

Figure 9 shows a diagram of the laser-wire beamline apparatus. A parallel laser beam (third-harmonic YLF,  $\lambda = 350$  nm) is transported from a laser shack (not shown) to the apparatus, where it passes across the beam path onto a focusing mirror which forms the waist. The spent light is then absorbed by glass absorbers. This arrangement was utilized in order to permit 1% of the laser light to be transmitted through the focusing mirror and re-imaged for diagnostic purposes. In addition, because the incoming light fills a significant fraction of the beampipe it is easier to locate with the electron beam than the light at the laser waist; this permits an unfocused electron beam to be used to adjust the collision timing with the incoming laser light.

In order to measure small electron spots, the waist of the laser must be smaller than the smallest electron beam size which is anticipated. At the same time, the depth of the focus should be relatively large so that the sensitivity of the vertical size measurement to the horizontal position of the beam is minimized. These two constraints, coupled with the space limitations of the installation, set most of the critical parameters of the design.

The minimum transverse RMS size of a diffraction-limited laser beam is:

$$\sigma_f = \frac{\lambda f}{4\pi\sigma_{in}}, \quad (7)$$

where  $f$  is the focal length of the lens and  $\sigma_{in}$  is the incoming laser beam RMS size. In practice the value of  $\sigma_{in}$  is limited by the acceptance of the laser transport and of the focusing mirror, while  $f$  is limited by the beampipe aperture. The rayleigh range is the distance over which a focused laser beam diverges to  $\sqrt{2}$  times its focused size, and is given by:

$$z_R = \frac{4\pi\sigma_f^2}{\lambda}. \quad (8)$$

In order to simultaneously achieve  $\sigma_f < 400$  nm and  $z_R \geq 5\mu\text{m}$  in the space allowed, it was necessary to use the near-UV third-harmonic YLF laser selected.

For a 45.6 GeV electron beam and 350 nm laser wavelength, the spectrum of

emitted photons is shown in Figure 10, and the peak photon energy is 25 GeV. If we consider a vertical size scan, the number of photons emitted as a function of the beam vertical position is given by:

$$\langle N_\gamma \rangle = \frac{P_L \sigma_C}{ch\nu_0} \frac{1}{\sqrt{2\pi}\sigma_s} \exp\left(\frac{-y^2}{2\sigma_s^2}\right) \int_{-\infty}^{\infty} dz \frac{1}{\sqrt{2\pi}\sigma_f} \exp\left(\frac{-z^2}{2\sigma_f^2}\right), \quad (9)$$

where we have written the power density in terms of the laser power  $P_L$  and assumed the laser power is Gaussian-distributed in  $y$  and  $z$ ; and where  $\sigma_s$  is the overlap size of the electron beam and laser beam at the waist,  $\sigma_s^2 \equiv \sigma_y^2 + \sigma_f^2$ . If we assume a vertical RMS electron beam size of 1 micron and the laser parameters above, the Compton cross section is  $3.47 \times 10^{-25} \text{ cm}^2$ , and the expected number of photons when the electron beam is at the laser waist is approximately 8000 for a peak laser power of 10 MW. Note that this is a slight overestimate: the beam has a horizontal RMS size of a few microns, which means that some particles are displaced from the laser waist and encounter a correspondingly lower photon density. This effect is on the order of 10%. The photon critical angle is 17 microradians, while the electron beam divergence is typically close to 300 microradians.

The outgoing beams from the SLC IP enter the opposing final focus, where there are several strong bends. This allows the primary beam to be separated from the 25 GeV photon beam and the 20 GeV recoil electrons. Either electrons or photons may be collected to form the signal for the beam size measurement. Figure 11 shows a measurement of the beam size using degraded electrons for the signal.

It is worth noting that, for a physically-realizable installation, the minimum achievable laser waist size (and therefore the smallest beam size measurable) for such a laser wire is typically on the order of the laser wavelength. Future linear colliders will have much more intense beams than even the SLC beam at the IP (with up to  $10^{12}$  particles per machine pulse and typical linac beam sizes from 1 to 10 microns [29]), and it is anticipated that laser wires will be the standard beam size monitor for most locations. However, laser wavelengths below 250 nanometers (fourth-harmonic YAG or YLF) will be difficult or impossible to achieve with the reliability required for beam diagnostics, and so for spot sizes smaller than 250 nanometers other approaches must be used.

## 4 BEAM SIZE MEASUREMENT USING LASER INTERFEROMETER

The general principle of laser-interferometric beam size measurements is illustrated in Figure 12: a single laser beam is introduced into a resonant cavity, resulting in a standing wave pattern in the electromagnetic field [27]. The fringe spacing of the standing-wave pattern is half the wavelength of laser light used: a first-harmonic YAG laser,  $\lambda = 1064 \mu\text{m}$ , generates a pattern with 532 nm spacing.

Now consider an electron beam which is scanned across the interference pattern. If the beam size is large relative to the fringe spacing, the core of the beam always intercepts several nulls and peaks of the interference pattern; consequently the number of photons which the beam will Compton-scatter is only a weak function of the electron beam position. If the beam size is very small relative to the fringe spacing, the number of Compton-scattered photons is a strong function of the electron beam position: for a dimensionless beam, the maximum number of photons are scattered when the beam intercepts a bright fringe while no photons are scattered when the beam intercepts a null. In general the number of scattered photons as a function of position is given by  $\langle N_\gamma \rangle = A + B \cos(2k_L x + \psi)$ , where  $k_L$  is the laser wave number and  $\psi$  an arbitrary constant. The ratio  $B/A$  is zero for an infinitely large beam and 1 for a dimensionless beam. It therefore follows that  $B/A$  is a function of the beam size, and that the beam size may be inferred from a measurement of  $B/A$ .

The system sketched in Figure 12 is not practical for several reasons, one of which is that the fringe spacing is always equal to half the wavelength of light selected. If the beam is too large or too small to be well measured by the system, the laser wavelength must be changed, which is not practical. Consider instead a system in which the incoming laser beam is split, and half the laser power is introduced into the interaction region at an angle  $+\phi$  relative to the horizontal, while the other half is introduced at an angle  $-\phi$ , as shown in Figure 13 [30]. If the wavenumber of the laser is given by  $k$  and the polarization of the laser is such that the magnetic field is in the  $xy$  plane while the electric field is parallel to the electron path (along  $z$ ), then

we find:

$$\begin{aligned}\vec{k}_1 &= k(\hat{x} \cos \phi + \hat{y} \sin \phi), \\ \vec{k}_2 &= k(\hat{x} \cos \phi - \hat{y} \sin \phi),\end{aligned}\tag{10}$$

while the magnetic field vectors of the two beams are given by:

$$\begin{aligned}\vec{B}_1 &= B \cos(\omega t - \vec{k}_1 \cdot \vec{r}) \hat{B}_1, \\ \vec{B}_2 &= B \cos(\omega t - \vec{k}_2 \cdot \vec{r}) \hat{B}_2, \\ \hat{B}_1 &= \hat{x} \sin \phi - \hat{y} \cos \phi, \\ \hat{B}_2 &= -\hat{x} \sin \phi - \hat{y} \cos \phi.\end{aligned}\tag{11}$$

When we compute the vector sum  $\vec{B}_1 + \vec{B}_2$  we find:

$$\vec{B}_1 + \vec{B}_2 = 2B[\hat{x} \sin \phi \sin k_y y \sin(\omega t - k_x x) + \hat{y} \cos \phi \cos k_y y \cos(\omega t - k_x x)],\tag{12}$$

where we have replaced  $k \cos \phi$  with  $k_x$  and  $k \sin \phi$  with  $k_y$ . Equation 12 shows that the interference of the two laser beams produces a standing wave pattern in the vertical and a travelling wave in the horizontal, and it also shows that the periodicity of the standing wave pattern is controlled by  $k_y$ , which is in turn a function of the crossing angle of the two beams. By varying the crossing angle, therefore, we may change the fringe spacing of the interference pattern and tune the pattern to measure beams of various sizes.

We can use Equation 12 to compute the value of  $\langle B_x^2 + B_y^2 \rangle$  as a function of  $y$ : since the wave is a travelling wave in the horizontal, we can replace all  $\sin^2(\omega t - k_x x)$  and  $\cos^2(\omega t - k_x x)$  terms with  $1/2$ , leaving:

$$\begin{aligned}\langle B_x^2 + B_y^2 \rangle &= B^2 [\sin^2 k_y y (1 - \cos 2\phi) + \cos^2 k_y y (1 + \cos 2\phi)] \\ &= B^2 (1 + \cos 2\phi \cos 2k_y y).\end{aligned}\tag{13}$$

From Equation 13 we see that the fringe spacing will be given by  $d \equiv \pi/k_y = \lambda_L/2 \sin \phi$ . For head-on laser collision,  $\phi = \pi/2$  and the spacing reduces to the familiar form for pure standing waves, while for smaller crossing angles the fringe spacing increases. Note, however, that the maximum modulation depth in Equation

13 is  $\cos 2\phi$ . Thus for head-on collisions the modulation depth of the fringe pattern is 100%, while for the special case of perpendicular laser beams ( $\phi = \pi/4$ ), the wave is purely travelling wave and no modulation is possible.

We can quantify the relationship between beam size and Compton-scattering modulation depth by convolving Equation 13 with the charge distribution of a Gaussian bunch, RMS size  $\sigma_y$ , centered at position  $y_0$ :

$$N_\gamma \propto \int_{-\infty}^{+\infty} \frac{1}{\sqrt{2\pi}\sigma_y} \exp\left[\frac{-(y-y_0)^2}{2\sigma_y^2}\right] (1 + \cos\theta \cos 2k_y y) dy, \quad (14)$$

where we have used the full crossing angle,  $\theta$ , in place of  $2\phi$ . Integrating this equation and replacing the average number of photons with  $N_0$ , we find [31]:

$$N_\gamma(y_0) = \frac{N_0}{2} \left\{ 1 + \cos 2k_y y_0 \cos\theta \exp\left[-2(k_y \sigma_y)^2\right] \right\}, \quad (15)$$

The maximum and minimum numbers of Compton scattered photons are given by:

$$N_+ = N_0/2(1 + \cos\theta...), \quad (16)$$

$$N_- = N_0/2(1 - \cos\theta...).$$

The ratio of the oscillation in Compton rate to the average rate,  $M$ , is given by:

$$\begin{aligned} M &\equiv \frac{N_+ - N_-}{N_+ + N_-} \\ &= |\cos\theta| \exp\left[-2(k_y \sigma_y)^2\right]. \end{aligned} \quad (17)$$

From Equation 17, we can estimate the spot size from the measured modulation depth:

$$\sigma_y = \frac{d}{2\pi} \sqrt{2 \ln\left(\frac{|\cos\theta|}{M}\right)}, \quad (18)$$

Figure 15 shows the modulation depth as a function of the beam size for a first-harmonic Nd:YAG laser with a crossing angle of  $174^\circ$  ( $d = 533$  nm). The largest beam which can reasonably be measured (at a modulation depth of 10%) is  $\sigma_y = 182$  nm, while the smallest beam which can reasonably be measured ( $M = 90\%$ ) has an RMS size of 38 nm. At the other extreme, a crossing angle of  $6^\circ$  can measure beam sizes from 3.5 microns down to 730 nm, with a 10.2 micron fringe spacing.

## 4.1 Systematic Effects

One of the useful features of the laser-interferometer technique is that most (though not quite all) systematic effects will tend to reduce the modulation depth, usually by increasing the number of Compton scatters which occur at a nominal null (through imperfections in the fringe pattern). Thus the measured beam size is usually an overestimate of the actual beam size. Several of the most important effects are discussed below.

### 4.1.1 LASER POWER IMBALANCE

Heretofore we have assumed that the laser power in the two interferometer arms is equal. If the power to the two arms is imbalanced, then the total fringe modulation is reduced. If the power in the two arms is given by  $P_1$  and  $P_2 \equiv P_1 P_I$ , then Equation 17 can be modified to show that:

$$\begin{aligned} M &= C_P |\cos \theta| \exp \left[ -2(k_y \sigma_y)^2 \right] \\ &= C_P M_{\text{ideal}}. \end{aligned} \tag{19}$$

where  $P_I$  is the relative power-imbalance factor and  $C_P$  is the correction factor for the total modulation depth of the interference pattern:

$$C_P = \frac{2\sqrt{P_1 P_2}}{P_1 + P_2} = \frac{2\sqrt{P_I}}{1 + P_I}. \tag{20}$$

Figure 16 shows the value of  $C_P$  as a function of  $P_I$ . The correction to the fringe modulation is not a strong function of the power imbalance: a factor of 2 imbalance only results in a loss of 6.1% in the pattern modulation depth. The resulting error in beam size estimation is given by:

$$\frac{\delta \sigma_y}{\sigma_y} = \left( \frac{d}{2\pi \sigma_y} \right)^2 \frac{\delta C_P}{C_P}. \tag{21}$$

The error resulting from an error in determination of the power imbalance is a strong function of the measured beam size itself: for a 2% error in  $C_P$ , a 60 nm beam size measured in the apparatus described above will be overestimated by 4%, while a 75 nm beam size will only be overestimated by 2.6%.



#### 4.1.2 ELECTRON-BEAM CROSSING ANGLE

If the trajectory of the electron beam is not parallel to the plane of the fringes, as shown in Figure 19, the beam will pass through the interference pattern at an angle. In this case the modulation in the Compton-scattered photons is reduced and the apparent beam size is increased. For a crossing angle  $\alpha$ , the apparent increase in measured beam size is given by:

$$\sigma_{\text{meas}}^2 = \sigma_y^2 + \alpha^2 \sigma_z^2, \quad (22)$$

where  $\sigma_z$  is the RMS longitudinal size of the laser.

#### 4.1.3 LONGITUDINAL EXTENT OF INTERFERENCE PATTERN

The interference pattern formed by the laser has a nonzero longitudinal extent, and while most photons are Compton-scattered at the core of the pattern where the intensity is highest some will also scatter off the upstream and downstream extremes of the interference pattern. If the beam size at the core is not equal to the beam size at the extremes, there will be some averaging of the measurements in different regions.

As one example, consider the situation in Figure 18: the electron beam's waist is at the  $z$  location of peak laser intensity, but the beam divergence causes the beam to be larger at the upstream and downstream extrema of the pattern. In this case, to good approximation the measured beam size  $\sigma_{\text{meas}}$  is related to the actual beam size  $\sigma_y$ , the RMS laser size  $\sigma_z$ , and the RMS electron beam divergence  $\sigma_{y'}$ , as follows:

$$\begin{aligned} \sigma_{\text{meas}}^2 &\approx \sigma_y^2 + \sigma_{y'}^2 \sigma_z^2 \\ &= \sigma_y^2 + \left( \frac{\sigma_y}{\beta_y^*} \right)^2 \sigma_z^2, \end{aligned} \quad (23)$$

where  $\beta_y^*$  is the vertical betatron function at the focal point of the electron beam. To measure the electron beam size with good accuracy, the laser beam size has to be smaller than half the betatron function. For  $\sigma_z = \beta_y^*/2$ ,  $\sigma_{\text{meas}} = 1.1\sigma_y$ .

#### 4.1.4 LASER PATHWAY ALIGNMENT

Because the laser intensity is Gaussian-distributed in  $x$  and  $z$ , it is important that the electron beam and the core of the two laser beams meet at a point in  $x$  and  $z$ .

In the case where one laser beam is aligned to the electron beam while the other is horizontally offset by  $\delta x$ , the effect on the modulation is given by:

$$M_{\delta x} = \frac{2 \exp\left(\frac{-\delta x^2}{4\sigma_L^2}\right)}{1 + \exp\left(\frac{-\delta x^2}{2\sigma_L^2}\right)} M_{\text{ideal}}, \quad (24)$$

where  $\sigma_L$  is the RMS transverse size of the laser. For an error  $\delta x = \sigma_L/2$ ,  $M = 0.998 M_{\text{ideal}}$ .

In the case where the two lasers are misaligned in  $z$  by an amount  $\delta z$ , the modulation becomes:

$$M_{\delta z} = \exp\left(\frac{-\delta z^2}{8\sigma_z^2}\right) M_{\text{ideal}}. \quad (25)$$

For an error of  $\delta z = \sigma_z/2$ ,  $M_{\delta z} = 0.97 M_{\text{ideal}}$ .

#### 4.1.5 SPATIAL COHERENCE OF THE LASER

If the spatial coherence of the laser is poor the wavefronts will not be planar, resulting in a non-planar interference pattern, as shown in Figure 20. This also reduces the measured modulation depth. In commercial high power YAG lasers, the laser beam is sometimes designed to fully cover the YAG-rod in order to maximize output energy in the light pulse. However, part of the power is cut and reflected from the edge, resulting in poor spatial coherence (profile) due to interference with the main beam. This must be avoided, and in general the optics of the laser transport must be designed with care to preserve the spatial coherence of the transmitted power.

An additional concern is the spherical wavefront error. The focusing or diverging laser beam is formed by spherical waves as shown in Figure 17. The spherical waves can only approximate plane waves (necessary to form a planar interference pattern) over a limited area around the focal point. The effect on modulation is given by:

$$M_{\text{measure}} = \left( \frac{2}{\sqrt{1 + \frac{2 \ln 2}{\pi} \frac{y}{z_R}}} - 1 \right) M_{\text{ideal}}. \quad (26)$$

For a first-harmonic YAG laser focused to an RMS size of 40  $\mu\text{m}$ , Equation 8 shows that  $z_R$  is 19 mm. At a distance of 2 mm from the focus point, therefore,  $M_{\text{measure}} = 0.95M_{\text{ideal}}$ .

#### 4.1.6 TEMPORAL COHERENCE OF THE LASER

Temporal coherence is essential for any kind of laser interferometry. If the coherence is poor the fringe contrast is reduced. The modulation is given by:

$$M_{\text{measure}} = \exp \left[ -\pi \left( \frac{\delta\nu\Delta l}{c} \right)^2 \right] M_{\text{ideal}}, \quad (27)$$

where  $\delta\nu$  is the line width and  $\Delta l$  is the path difference in the two laser pathways from the beam splitter to the collision point. To obtain the ideal modulation we have to choose a laser with a narrow line width or else make the path lengths equal in the interferometer design.

Another concern is the temporal profile of the laser pulse. The Nd:YAG laser has a wide natural line width, approximately  $1 \text{ cm}^{-1}$ . In Q-switch pulsed YAG lasers, many longitudinal modes are excited simultaneously and sharp spikes are generated in the output waveform due to interference of these modes. This increases the statistical scatter in the number of Compton-scattered photons.

In order to limit the number of longitudinal modes, it is essential to use injection seeding. A frequency stabilized solid-state laser injects a CW low power beam into the oscillator; when the Q-switch is opened the high power beam starts from this coherent wave. Such devices are commercially available, and can reduce the line width of a Nd:YAG laser to  $0.03 \text{ cm}^{-1}$ . The temporal profile becomes a Fourier-limited smooth waveform in this case.

#### 4.1.7 LASER JITTER

The laser-interferometer is subject to three forms of jitter which are significant on a shot-to-shot level: laser timing jitter, laser position jitter, and laser intensity jitter. Because the measurement of beam size takes many beam pulses, all forms of jitter must be held to acceptable levels. Note that laser jitter can cause a reduction in

intensity in the dark regions of the interference pattern as well as the bright ones, and therefore has the potential to reduce the measured beam size below the actual size.

High-powered lasers are usually operated in pulsed mode, and therefore they must be triggered such that the peak intensity of the laser light arrives at the interaction point at the same time as the electron beam. The jitter on laser triggering must be small relative to the length of the laser pulse.

Since the positioning of light and dark regions of the interference pattern is a function of the path length from the final mirrors of each pathway to the collision point, jitter of the incoming laser does not move the intensity pattern. However, the jitter can illuminate different parts of the pattern, as shown in Figure 21. Since the full modulation intensity is present only in a small region near the center of the pattern, this jitter must be small relative to the transverse laser size.

Finally, intensity jitter can change the apparent modulation depth by changing the overall intensity of the interference pattern when the electron beam passes through.

## **4.2 Laser-Interferometer Beam Size Monitor in the Final Focus Test Beam**

The Final Focus Test Beam (FFTB) is an experiment designed to test the optics and performance of a final focus system for future linear colliders. The FFTB beamline is located at the end of the SLAC linac, and is designed to demagnify the incoming 46.6 GeV beam to an RMS size of 1.7 microns (horizontal) by 60 nanometers (vertical). The demagnification from the beam size in the linac required to do this is the same as the demagnification foreseen in some future linear collider designs [32].

A vertical beam size of 60 nanometers is clearly beyond the measurement capabilities of any technology described above other than the Laser-Interferometer BSM. While the horizontal size of 1.7 microns is measurable by conventional wire scanners, the product  $\sigma_x\sigma_y$  is so small that for the FFTB's nominal bunch charge of  $1.0 \times 10^{10}$  electrons, a conventional wire would be destroyed immediately if it was employed to

measure the beam size. Thus a laser technique such as the Laser-Interferometer BSM is also required in the horizontal.

The design selected for the FFTB's focal point is diagrammed in Figure 22: a single first-harmonic Nd:YAG laser is employed, and three different operating modes are permitted. The first mode employs a  $174^\circ$  crossing angle to allow measurement of vertical beam sizes from 40 to 180 nm; the second mode uses a  $30^\circ$  crossing angle to allow measurement of vertical sizes from 160 to 720 nanometers; the third mode employs a  $6^\circ$  crossing angle in the horizontal, and is used to measure horizontal beam sizes from 0.76 to 3.4 microns [31]. The modulation depths for each mode as a function of beam size are shown in Figure 23. A total of 6 laser pathways enter the chamber where the collisions with the beam occur. For each mode the path lengths of the two pathways are equal to guarantee perfect modulation. The final mirror which guides the light into the chamber is connected to remote-controlled movers with 2 degrees of freedom, which allow real-time alignment of the laser positions at the IP. Initial alignment of the longitudinal position is performed using a slit with a  $z$  aperture of 500 microns, which is inserted into the laser pathway: each laser in turn is directed onto the slit (by opening and closing appropriate shutters), and detected by a photodiode opposite the laser entry point; the  $z$  mover is adjusted to the center position of the transmitted window. Alignment of the lasers in  $x$  and  $y$  is done directly to the electron beam: the shutters are closed to allow light from only one of the six pathways into the interaction chamber, and the electron beam is steered across the laser beam. The distance from the electron beam's nominal position to the position of peak Compton intensity is thus determined, and the laser light is then steered to the electron beam nominal position. This measurement also determines the relative intensity of each laser pathway, which in turn allows a correction for the unequal intensities as discussed in the previous section.

The laser selected was a commercially-available model which produces 200 mJ and a 10 ns total pulse length, with a repetition rate of 10 pulses per second. In order to improve the spatial profile, the oscillator mirror was selected to form a smaller diameter in the YAG-rod, which provides a smooth Gaussian profile but reduces the

power. The YAG laser oscillator is followed by an adjustable telescope which is used to control the beam size at the collision point. The laser pulse is then transmitted through a light pipe into the FFTB enclosure, and into the interferometer apparatus. Each laser pathway contains a single lens with a focal length of 1 meter which is followed by the vacuum window into the collision chamber. Any high-frequency spatial component in the incoming laser beam creates an image far from the axis, which does not interact with the electron beam. As the focal length of the final lens is long compared to the transverse size of the laser beam, the third-order non-spherical distortion is negligible. Over the lifetime of the experiment the laser size at the collision point was made as small as 25 microns and as large as 60 microns RMS. While the 25 micron size has better signal-to-noise performance and a reduced dilution due to the longitudinal size of the fringe pattern, it is more sensitive to alignment drifts. A compromise size of 40 microns was finally settled on. At the nominal bunch charge listed above, Equation 9 predicts a Compton flux of 850 photons for 40 micron RMS laser size. A splitter is used to direct 1% of the incident laser power to a CCD camera, whose image is sent to the accelerator control room and to the control software for the laser. The control room image allows users to verify that the laser shape is round, while the laser control system uses the digitized centroid position to control two mirrors which provide position feedback.

In the FFTB extraction line the electron beam is separated from the gamma rays by a series of soft vertical bends followed by a set of strong permanent magnet bends. A photomultiplier tube above the beamline downstream of the strong bends detects the photons, while a second detector is below the beamline detects the degraded electrons. Ultimately the photon detector was almost always used for the measurements: as Figure 8 shows, the electron spectrum contains a considerable contribution of particles which lose almost no energy and are not ejected by the bends, and therefore the electron signal tends to be poor compared to the photon signal.

One complication of the design is the considerable sensitivity to beam-induced backgrounds. The electron beam divergence at the focal point is quite large, and the apertures of nearby quadrupoles are quite tight. Unacceptable backgrounds can be

generated by a small number of electrons hitting the vacuum pipe in the magnets around the focal point, and in general the resulting beam loss is too small to detect with conventional loss monitors. The backgrounds are controlled through use of special strong-focusing optics in the quads of the extraction line, steering around the focal point, and use of collimators in the last few hundred meters of the linac to eliminate beam haloes [33], as well as a few adjustable collimators upstream in the FFTB.

Even with the careful attention to background described above, some irreducible sources of beam-induced background remain, including the synchrotron radiation from the quads. While the backgrounds are small relative to the peak signals (signal/noise ratio of 10 was routinely achieved), background counts would tend to enhance the Compton signal when the beam passed through the nulls of the interference pattern and enlarge the measured size. This is corrected by triggering the laser at 10 Hz while the electron beam is run at 30 Hz. For each pulse with the laser present, the detected signal on the preceding and following pulses (with no laser present) are used to estimate the background, which is subtracted. On each step of the beam position, 6 beam pulses with the laser and 12 pulses without the laser are combined to produce one reading. A full measurement of 50 steps of the beam position thus takes 900 pulses, or 30 seconds. Figure 24 shows a beam size measurement without background subtraction, and the same measurement with background subtraction.

### 4.3 Use of the Laser-Interferometer BSM at the FFTB

Figure 25 shows a horizontal spot size measurement performed with the Laser-Interferometer BSM set to its third mode. The modulation depth is  $47.7 \pm 2.3\%$ , corresponding to a beam size of  $1.95 \pm 0.06$  microns.

Figure 26 shows a horizontal spot size measurement performed with the Laser-Interferometer BSM set to its second mode, used for larger vertical spot sizes. The modulation depth is  $82.6 \pm 2.9\%$ , corresponding to a beam size of 90 nm. Note that the modulation depth is within experimental error of the maximum achievable for this mode (86.6%).

Figure 27 shows a vertical spot size measurement performed with the Laser-Interferometer BSM set to its first mode, used for the smallest vertical spot sizes. The modulation depth is 66%, corresponding to a beam size of 77 nm. The estimated statistical error on the beam size measurement is 7 nm. Figure 28 shows the distribution of spot size measurements made over a 3 day period in December of 1997.

Achieving the smallest measured spot sizes requires a certain amount of “bootstrapping” because of the limited dynamic range of the vertical beam size modes and the large angular divergence of the electron beam. In general, if the waist position and the laser collision point differed by 0.5 mm in  $z$ , the beam was too large to measure with the smallest mode. Initially the second measurement mode was set up and a difficult program of multidimensional parameter scanning was performed to achieve the first measurement of vertical size, after which the tuning proceeded quickly. In later periods, a high-resolution beam position monitor near the IP [34] was utilized in the following way: the waist position and other aberrations were tuned to minimize the pulse-to-pulse jitter measured by the BPM, at which time the waist was moved by the distance from the BPM to the BSM. This procedure assumes that the jitter envelope and the beam envelope are reasonably similar in shape, which is not *a priori* obvious; nonetheless, in practice the procedure always converged quickly.

While beam sizes as small as 58 nm were measured with the Laser-Interferometer BSM, the focused electron beam size was typically measured to be 70 nm. Given the excellent performance of the SLAC linac during FFTB runs, the expected size is actually closer to 40 nanometers, even smaller than the design size. This is attributable, at least in part, to electron beam jitter at the focal point. The incoming jitter envelope has been measured, and its contribution to the expected jitter at the focal point is only 15 nanometers; nonetheless, direct measurements of the jitter indicate that the relative jitter between the beam and the fringe pattern are closer to 40 nm [35]. This is consistent with the measured vibrations of the strong quadrupoles upstream of the focal point (due to cooling water ground noise, and so on) and the predicted response of the beam to the vibrations. While the Laser-Interferometer BSM is mounted on the table which holds the quads, it is noted above that moving



the laser and the interferometer relative to one another does not change the position in space of the bright and dark lines in the interference pattern. Thus the beam was jittering while the interference pattern was fixed in its path. Options for correction of the jitter and/or direct measurement of same are underway.

#### **4.4 Ultimate Limits of Laser-Interferometer BSM Technique**

The existing Laser-Interferometer BSM installation was designed to meet the requirements of the FFTB experiment. Future projects, such as future linear colliders, will have different requirements and likely will need to measure smaller spot sizes. At this time variations on the Laser-Interferometer BSM seem like the best way to make such measurements.

The fundamental limit on the measured beam size is the wavelength of laser light selected. As described above, first-harmonic Nd:YAG lasers cannot be used for measurements below 40 nanometers. Frequency-doubled and frequency-tripled lasers are in common use today and these would permit measurements down to 13 nanometers, while the less-common frequency-quadrupled lasers would conceivably permit beam sizes as small as 10 nm to be measured, and could measure 20 nm spot sizes with ease. Such a laser would have a wavelength of 266 nm, well into the ultraviolet; this has considerable implications on the availability of optics components, and increases the risk of component damage.

Even a frequency-quadrupled laser will not permit direct measurement of the beam sizes required for some future linear colliders, which are as small as 3 nm. In addition, it will be difficult to make a Laser-Interferometer BSM which can be installed at or near the interaction point of a linear collider due to interference with the particle physics detector. Such high-resolution beam size monitors are thus unlikely to be installed at the interaction point itself, but rather they would likely be at an upstream image point of the IP, and used for tuning the incoming beam.

The secondary limitation on beam size measurement is the jitter issue discussed above. This can be resolved in two ways: either eliminate the vibration of the magnets which drive the beam jitter (via an optical anchor, for example), or measure the jitter

with high-resolution BPMs and subtract its contribution to the beam size. For an image point of the IP, the jitter is likely to be less important since there will not be strong quads in the vicinity.

## 5 CONCLUSIONS

A wide variety of technologies are available for the measurement of transverse beam sizes at high energies. The simplest technique is a profile monitor, which can measure beam sizes down to a few tens of microns RMS and can perform a measurement on a single pulse; however, profile monitors are invasive and subject to difficulties in image digitization. For beam sizes down to 1 micron wire scanners can be used, and usually these can be made non-invasive. The primary drawbacks of wire scanners are long measurement times, more complex timing than profile monitors, and the possibility of damaging the scanner with the beam.

An unbreakable target for beam size measurements is the photons in a laser, which are Compton-scattered into the beam-forward direction and detected. The most straightforward use of a laser is to use a diffraction-limited, finely focused laser to take the place of a metal wire. Such “laser wire” scanners have been built and used, and can be used to measure beam sizes down to 0.25 microns.

For still smaller sizes, one can use a laser to form an interference pattern in the path of the beam. The number of Compton-scattered photons are measured as a function of beam position in the interference pattern, and the modulation depth of the resulting sinusoidal distribution reveals the size of the electron beam. One such device, installed at the Final Focus Test Beam at SLAC, used a first-harmonic Nd:YAG laser ( $\lambda = 1.064$  microns) to measure beam sizes down to 60 nanometers, with a theoretical ultimate resolution limit of 40 nanometers. Such a complex device requires considerable care in design and implementation to avoid deleterious systematic effects in the fringe pattern, but the FFTB monitor was repeatedly and reliably used for measuring beams with an RMS size under 100 nm.

Through use of second-, third-, or fourth-harmonic lasers, the achievable resolution

can be improved by a similar factor, allowing 10 nm beam sizes to be measured. This potentially requires improvements in the control or measurement of beam jitter induced by magnet vibration. This is foreseen as a possible diagnostic tool in future linear colliders.

## 6 ACKNOWLEDGEMENTS

The authors would like to acknowledge the assistance of the following people: at SLAC, D. Burke, F.-J. Decker, C. Field, R. Iverson, D. McCormick, M. Ross, S. Wagner, D. Walz; at KEK, K. Oide, N. Yamamoto; at KAWASAKI Heavy Industry, A. Hayakawa, Y. Ozaki.

This work was supported by the Department of Energy under contract DE-AC03-76SF00515.

## References

- [1] Ross, MC et al. *Proc. 4th AIP Wkshp. Accel. Inst.*, ed. JA Hinkson, G Stover. New York:AIP Press (1993) pg 264
- [2] Field, C. *Nucl. Inst. Meth. A* 360:467 (1995)
- [3] Carey, DC. *The Optics of Charged Particle Beams*. Chur:Harwood (1987) pg 99
- [4] Wiedemann, H. *Particle Accelerator Physics*. Berlin:Springer-Verlag (1993) pg 152
- [5] McDonald, KT, and Russell, DP. In *Frontiers of Particle Beams; Observation, Diagnosis, and Correction*, ed. M Month, S Turner. New York:Springer-Verlag (1989) pg 122
- [6] Fewell, N, and Witkover, R. *Proc. Proton Lin. Acc. Conf.*, ed. KH Harper. Springfield:National Technical Information Service (1972) pg 54
- [7] Raimondi, P et al. *Proc. Int. Conf. High Energy Accel. 17*. In press

- [8] Raubenheimer, T, Yokoya, K. *Proposed ILC Parameters. LCC-Note-0003*. Stanford Linear Accelerator Center, Stanford, California, USA (1998) pg 2
- [9] Allison, RW et al. *A Radiation Resistant Chromium Activated Aluminum Oxide Scintillator. UCRL-19270*, Univ. Calif. Berkeley, Berkeley, Calif. (1969)
- [10] Bosser, J et al. *Nucl. Inst. Meth. A* 238:45 (1985)
- [11] Graves, WS, Johnson, ED, Ulc, S. *Proc Beam Inst. Wkshp 8*, ed. RO Hettel, SR Smith, JD Masek. New York:AIP Press (1998) pg 206
- [12] Yencho, S, Walz, D. *Proc. 1985 Part. Accel. Conf.* Piscataway:IEEE Press (1985) pg 2009
- [13] Decker, F-J, Brown, R, Seeman, JT. *Proc. 1993 Part. Accel. Conf.* Piscataway:IEEE Press (1993) pg 2507
- [14] Gannon, J et al. *Proc. 1989 Part. Accel. Conf.* Piscataway:IEEE Press (1989) pg 68
- [15] Ross, MC. *Proc. Wkshp. Accel. Inst. 2*, ed. ES McCrory. New York:AIP Press (1991) pg 88
- [16] McCormick, D et al. *Proc Beam Inst. Wkshp 6*, ed. GH Mackenzie, B Rawnsley, J Thomson. New York:AIP Press (1995) pg 391
- [17] Field, C, McCormick, D, Raimondi, P, Ross, M. *Proc Beam Inst. Wkshp 8*, ed. RO Hettel, SR Smith, JD Masek. New York:AIP Press (1998) pg 440
- [18] Bambade, P, Erickson, R. *Proc. 1986 Lin. Accel. Conf.*, ed. F Bennett, J Kopta. Stanford:SLAC (1986) pg 475
- [19] Raimondi, P, Decker, F-J. *Proc. 1995 Part. Accel. Conf.* Piscataway:IEEE Press (1996) pg 2922
- [20] Seeman, JT. *PEP-II Machine Advisory Committee Meeting, December 14-16, 1998*, ed. JT Seeman (1998)

- [21] Bovet, C, et al. *Proc. Europ. Part. Accel. Conf. 5*, ed. S Myers et al. Bristol:Institute of Physics Publishing (1996) pg 325
- [22] Emma, P, Hendrickson, LJ, Raimondi, P, Zimmermann, F. *Proc. 1997 Part. Accel. Conf.* In press
- [23] Brinkmann, R. *Determination of HERA Specific Luminosity from Beam Separation Scans. DESY Tech. Note HERA 94-03*. Deutsches Elektronen-Synchrotron, Hamburg, Germany (1994)
- [24] Heitler, W. *The Quantum Theory of Radiation*. Oxford:Clarendon (1954)
- [25] Ginsburg, IF, Kotkin, GL, Serbo, VG, Telnov, VI. *Sov. J. Nucl. Phys.* 38(2):222 (1983)
- [26] Telnov, VI. *Nucl. Inst. Meth. A* 294:72 (1990)
- [27] Shintake, T. *Nucl. Inst. Meth. A* 311:453 (1992)
- [28] Ross, MC et al. *Proc. Beam Inst. Wkshp. 7*, ed. AH Lumpkin, CE Eyberger. New York:AIP Press (1997) pg 281
- [29] Kuhlman, S et al. *Physics and Technology of the Next Linear Collider*. Stanford:SLAC (1996) pg 150
- [30] Shintake, T. *Proc. Beam Inst. Wkshp. 7*, ed. AH Lumpkin, CE Eyberger. New York:AIP Press (1997) pg 130
- [31] Shintake, T et al. *Proc. Int. Conf. High Energy Accel. 15*, ed. J Rossbach. Singapore:World Scientific (1993) pg 215
- [32] Oide, K. *Proc. 1989 Part. Accel. Conf.* Piscataway:IEEE Press (1989) pg 1319
- [33] Jacobsen, R et al. *Proc. 1991 Part. Accel. Conf.* Piscataway:IEEE Press (1991) pg 834
- [34] Slaton, T, Mazaheri, G, Shintake, T. *Proc. 1998 Lin. Accel. Conf.* (1998) In press

- [35] Woods, M, Kotseroglou, T, Shintake, T. *Vertical Position Stability of the FFTB Electrom Beam Measured by the KEK BSM. FFTB-Note 98-03*. Stanford Linear Accelerator Center, Stanford, California, USA (1998)

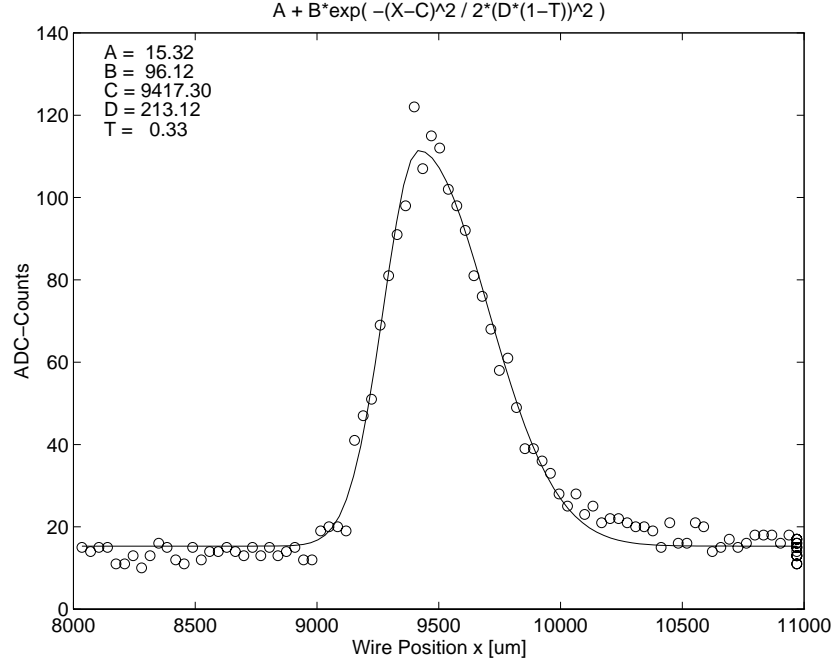


Figure 1: Example of a beam with a non-Gaussian transverse profile due to wakefields. The wakefields cause the tail to be deflected to one side; as a result that side of the transverse profile appears “wider.” The beam in the figure has a 33% asymmetry, and was measured with a wire scanner: measured signal (circles) and asymmetric-Gaussian fit (solid) are shown.

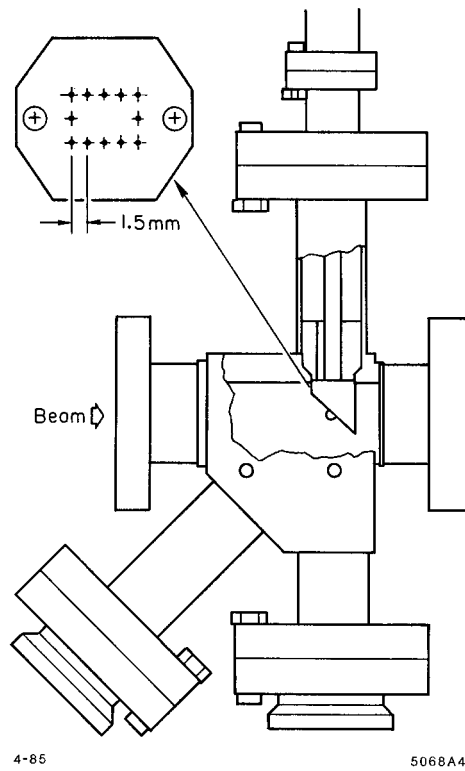


Figure 2: Schematic of a profile monitor. The beam passes through a sheet of material which emits light due to scintillation, transition or Cherenkov processes, or other effects. The screen is imaged by a camera and transported to a user or a digitizer.



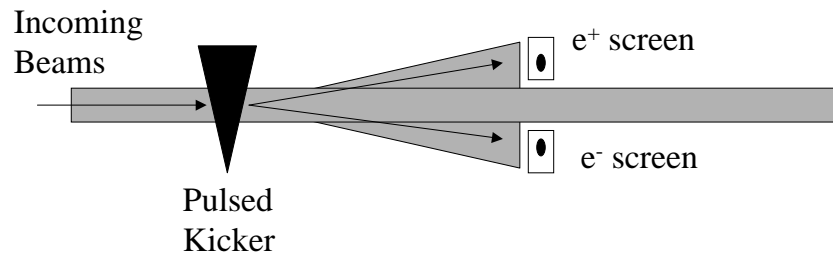


Figure 3: Non-invasive profile monitors used at the end of the SLAC linac. A pulsed kicker deflects the electron and positron beams onto separate off-axis screens, whose images are digitized and transmitted to the control room. This allows profiles to be captured without inserting a screen into the path of the main beam.

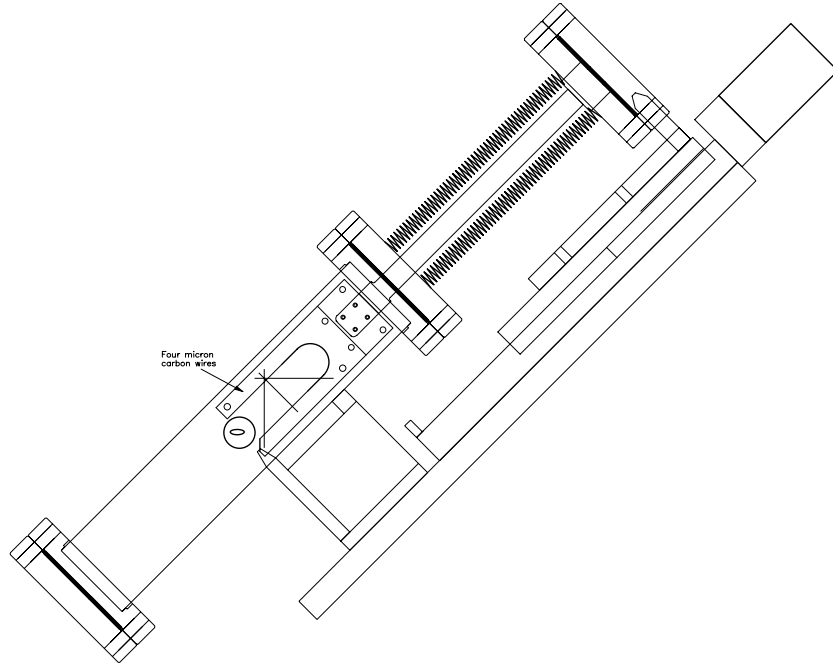


Figure 4: Diagram of a wire scanner.

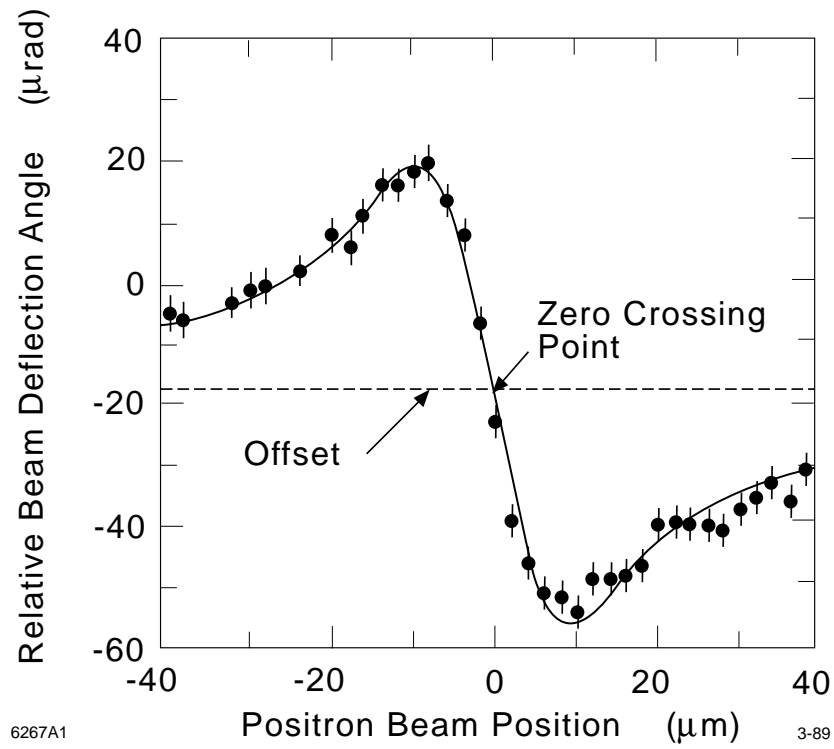


Figure 5: A beam-beam deflection scan: the deflection of one beam is plotted as a function of the separation of the two beams at the IP.

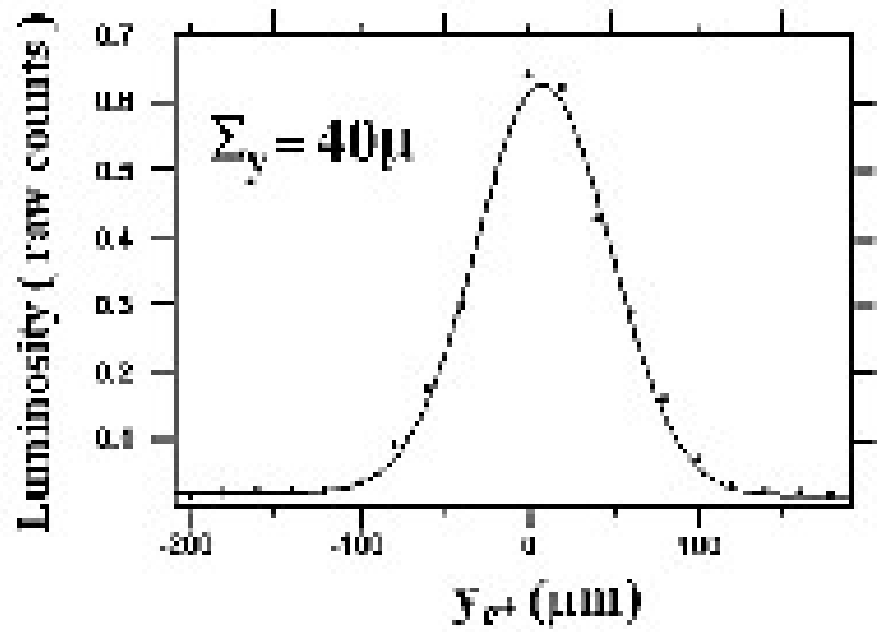


Figure 6: A beam-beam luminosity scan: the signal from a luminosity signal is plotted as a function of the beam-beam offset at the IP, produced by a local bump. The RMS width, 40 microns, is the convolved size of the two beams. Figure courtesy Diane Rogers, SLAC.

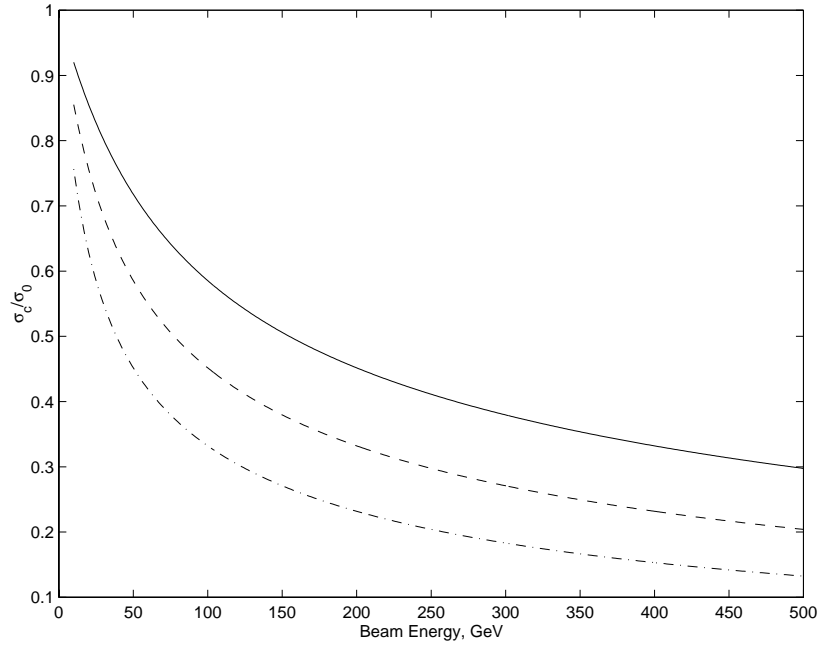


Figure 7: Ratio of Compton to Thompson cross-section,  $\sigma_c/\sigma_0$ , as a function of beam energy for a Nd:YAG laser operated at first (solid), second (dashed), or fourth (dot-dash) harmonic.

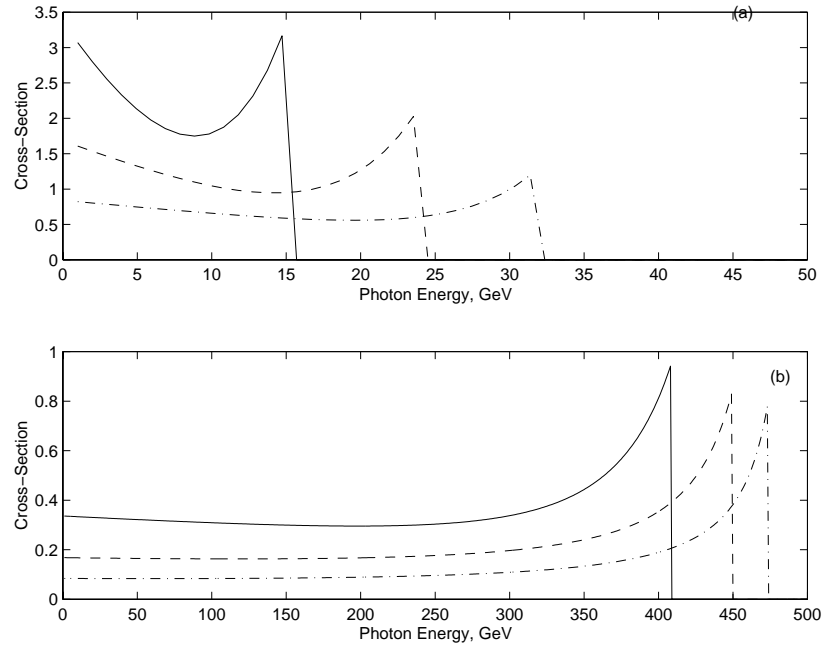


Figure 8: Spectrum of Compton-scattered photons from a 50 GeV (top) or 500 GeV (bottom) electron beam. The spectrum is shown for a Nd:YAG laser at first (solid), second (dashed), or fourth (dot-dash) harmonics.

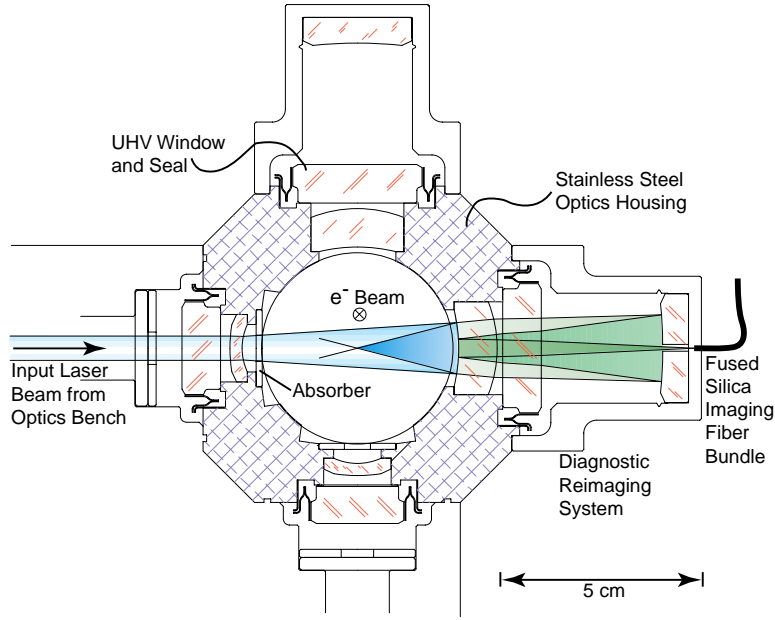


Figure 9: Schematic of SLC/SLD IP laser wire. Light enters at left, is focused by a spherical mirror on the right, and collides with the electron beam in the center. Approximately 1% of the laser power is transmitted through the focusing mirror and reimaged for diagnostic purposes on the far right. The scan is performed by sweeping the beam via upstream corrector magnets.

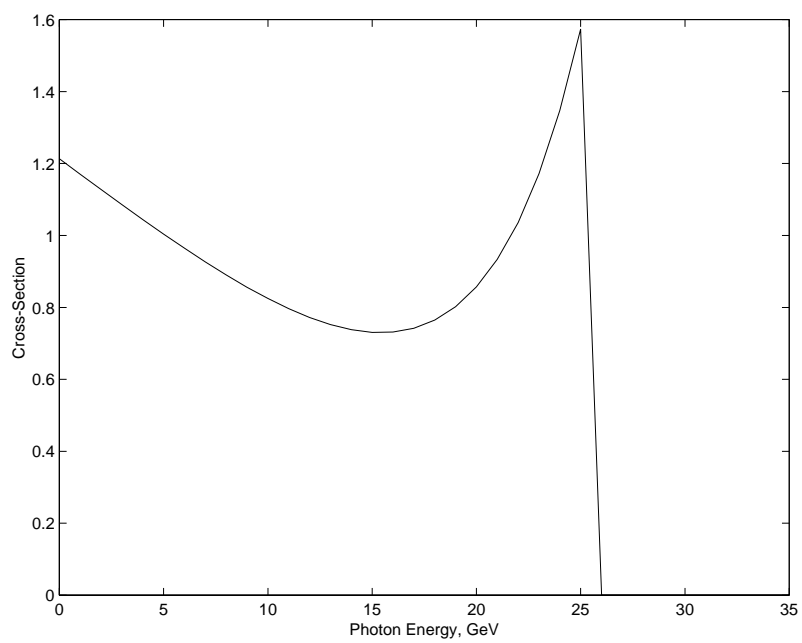


Figure 10: Spectrum of Compton-scattered photons from the SLC/SLD laser wire.

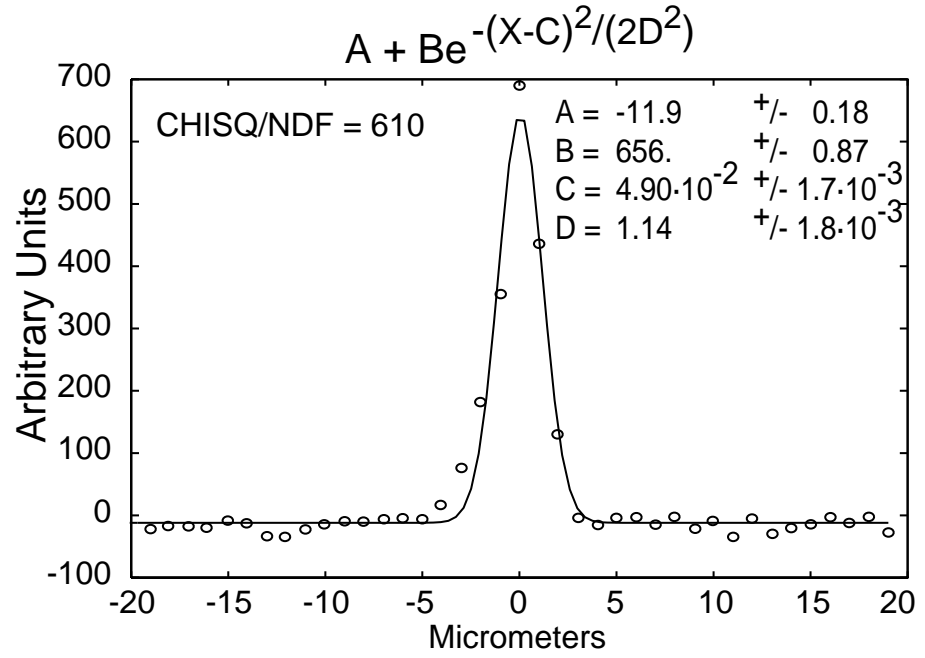


Figure 11: Measurement of the beam transverse size via the laser wire. The measured beam size is approximately 1 micron.



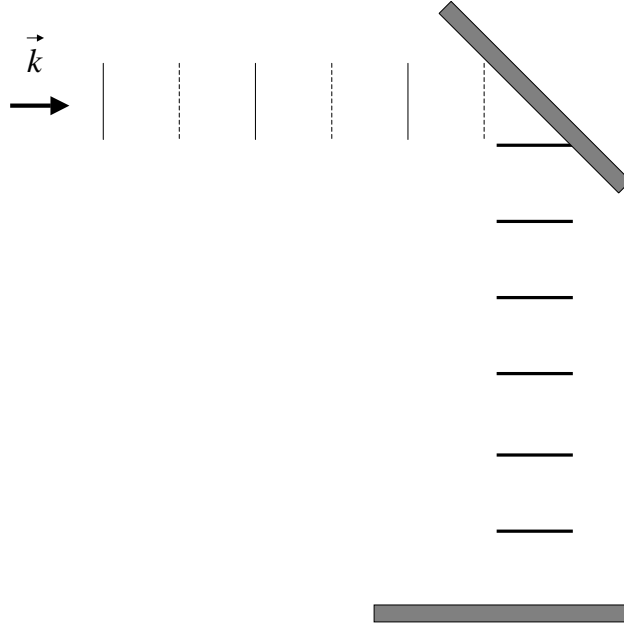


Figure 12: Diagram of simple laser interferometer for beam size measurement. A laser with wave vector  $\vec{k}$  is introduced into a resonant cavity. The resulting standing wave pattern has intensity maxima (dark solid lines) whose spacing is half the wavelength of the incoming laser (solid lines are maxima, dashed lines are minima).

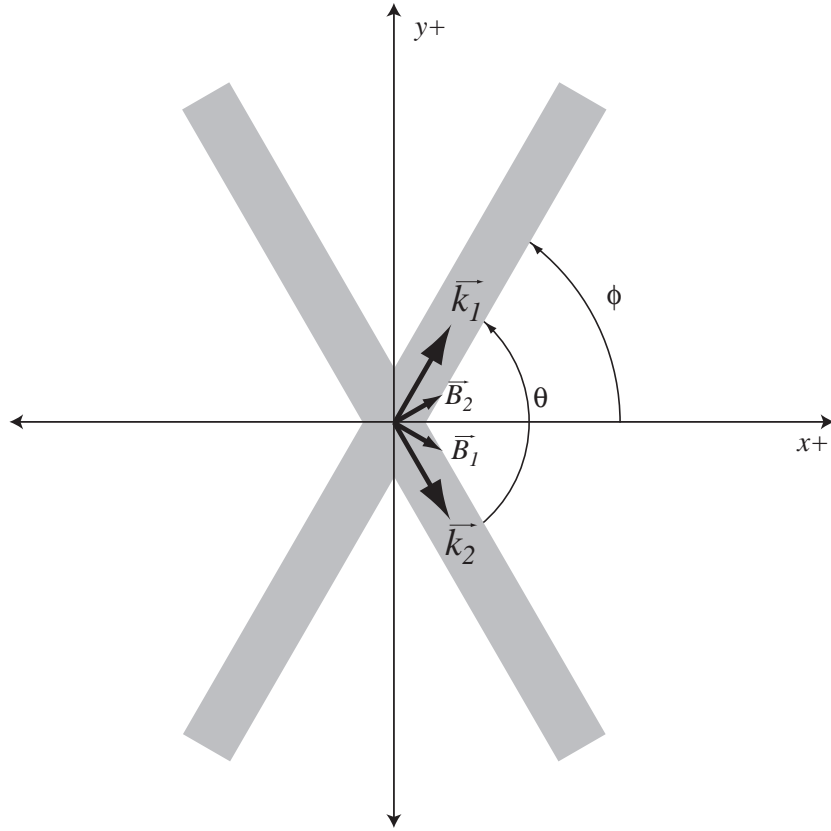


Figure 13: Diagram of 2 lasers intersecting at an angle  $\theta$ ; the magnetic field vectors and momentum vectors are shown.

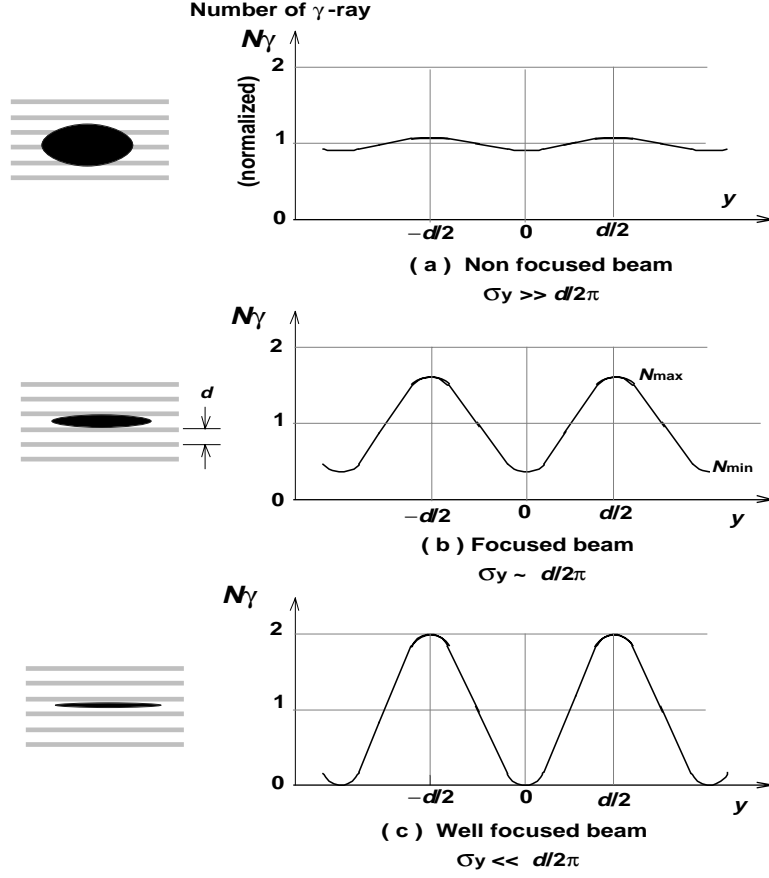


Figure 14: Use of laser-interferometer to measure a beam size. A beam which is large relative to the fringe spacing does not produce modulation in the intensity of Compton-scattered photons as it is scanned across the interference pattern (top); a beam which is very small relative to the fringe spacing produces nearly 100% modulation (bottom).

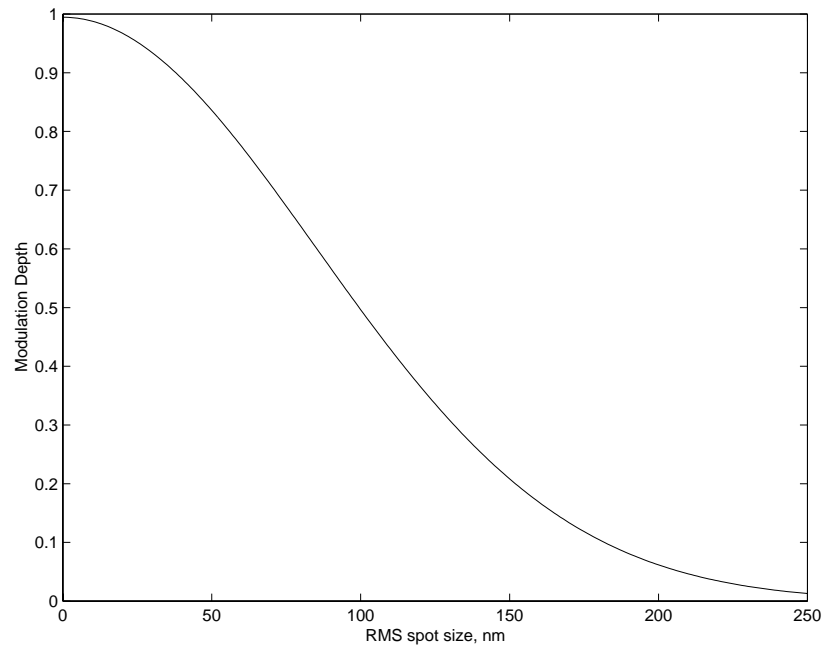


Figure 15: Modulation depth as a function of beam size for laser-interferometer beam size monitor with laser crossing angle of  $174^\circ$ . The range of the monitor is from 40 nm to 180 nm.

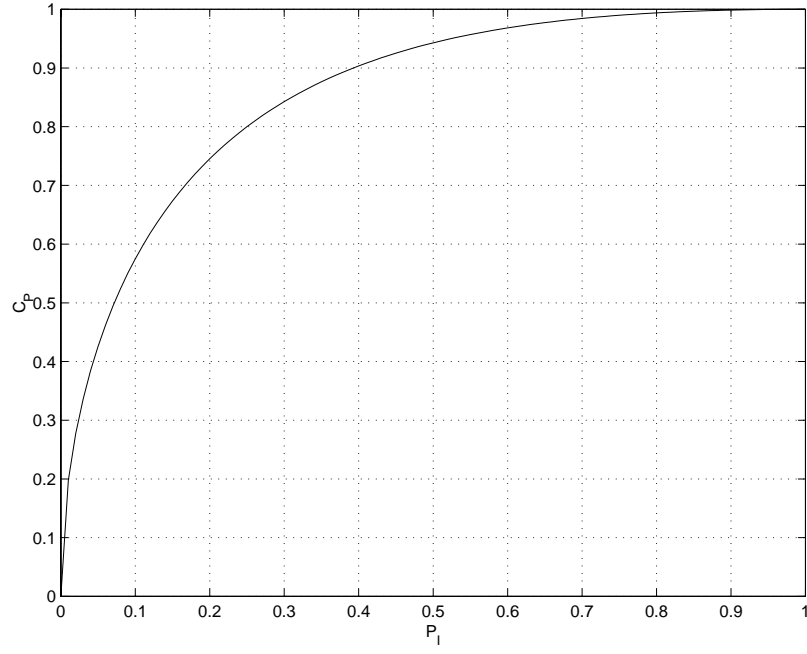


Figure 16: Relationship between power imbalance factor,  $P_I$ , and fringe contrast,  $C_P$ . Perfectly balanced laser power in the two interferometer arms corresponds to  $P_I = 1$ . Note that  $C_P$  is a weak function of  $P_I$ : a 2:1 power imbalance only results in a reduction in contrast of 6%.

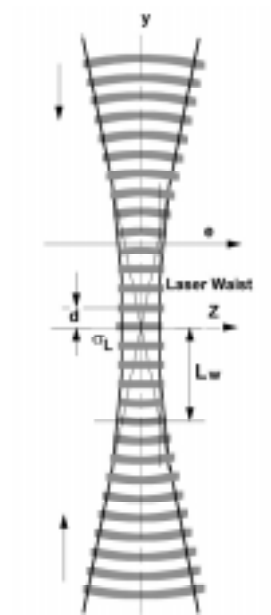


Figure 17: Diagram of spherical wavefront error. The wavefronts of a focused laser are only planar to good approximation within a fraction of the Rayleigh range.

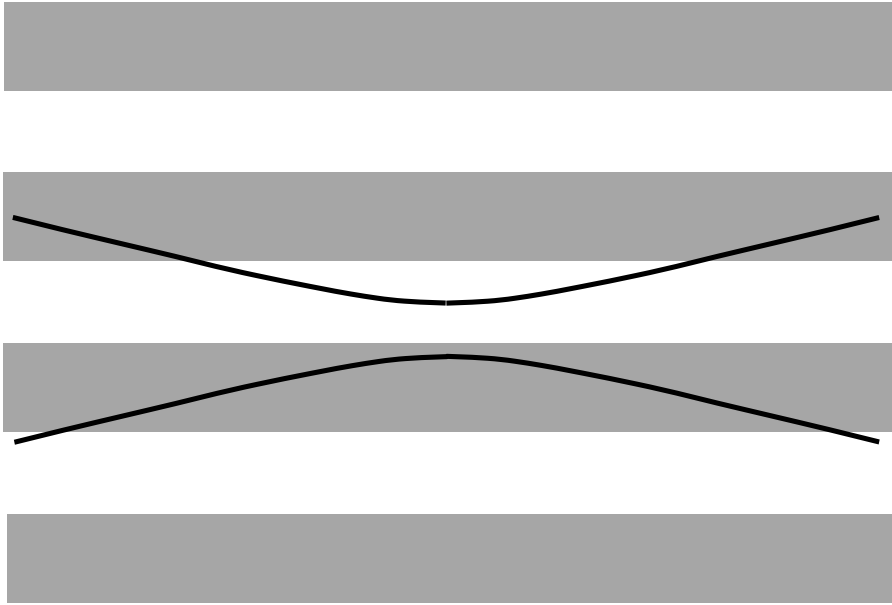


Figure 18: Overlap of the beam envelope function (black) with the interference fringes (grey). The beam size is changing over the longitudinal extent of the interference pattern; consequently the rate of Compton scattering will average over the focused part of the beam at the center of the pattern and the unfocused portion near the extremes. This will dilute the measured modulation depth, as discussed in the text.

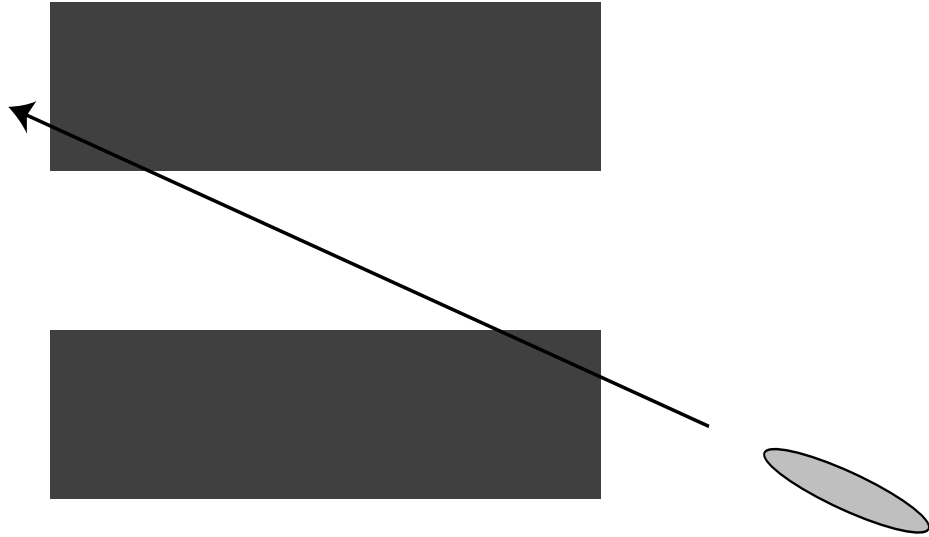


Figure 19: A beam passing through the interference pattern with a crossing-angle. Because the beam passes through light and dark regions of the pattern, the measured modulation depth is reduced.



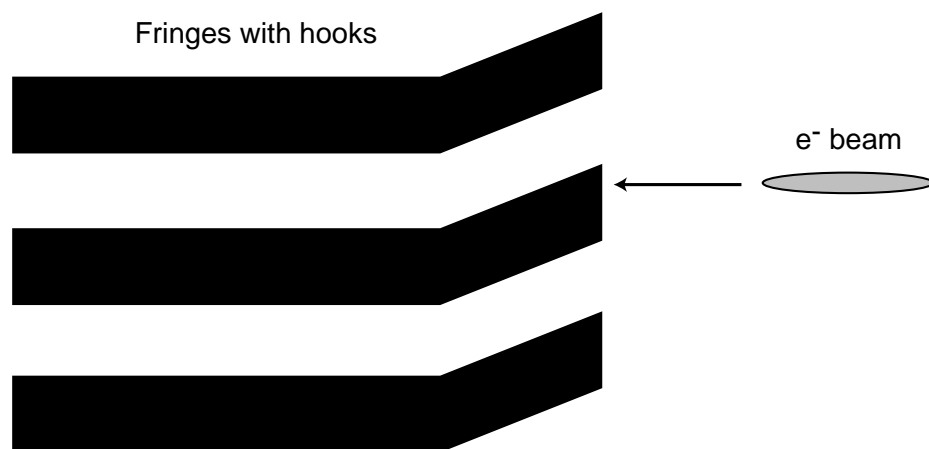


Figure 20: Effect of poor spatial coherence of the laser. The interference fringes become distorted in space, with “hooks” appearing on the fringes. These hooks tend to add intensity to the dark parts of the interference pattern, reducing the modulation depth.

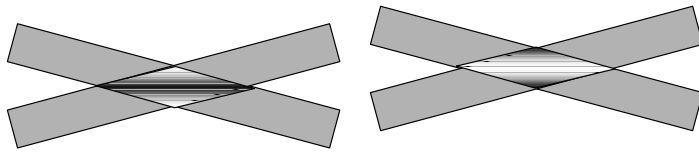


Figure 21: Effect of laser position jitter (or monitor installation jitter) on the interference pattern. The pattern does not move in space; however, the fringe which has the maximum intensity may change.

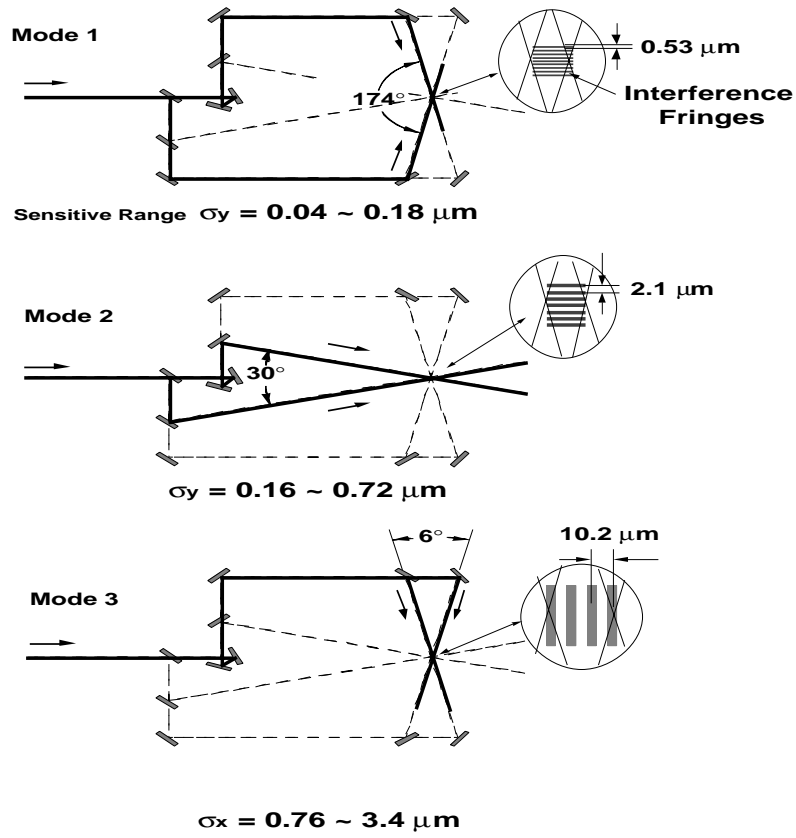


Figure 22: Diagram of the laser-interferometer beam size monitor installed in the Final Focus Test Beam. Use of 3 different crossing angles allows measurement of both large and small vertical beam sizes as well as horizontal sizes.

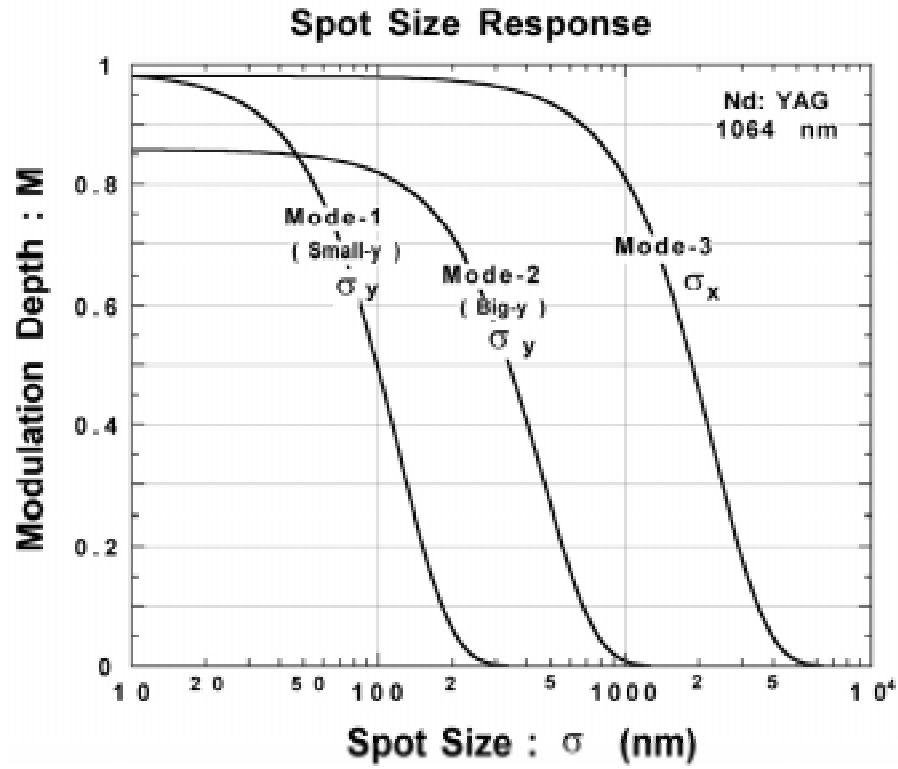


Figure 23: Modulation depth as a function of beam size for the 3 modes of the FFTB laser-interferometer beam size monitor: crossing angles of 174°, 30°, and 6° are shown.

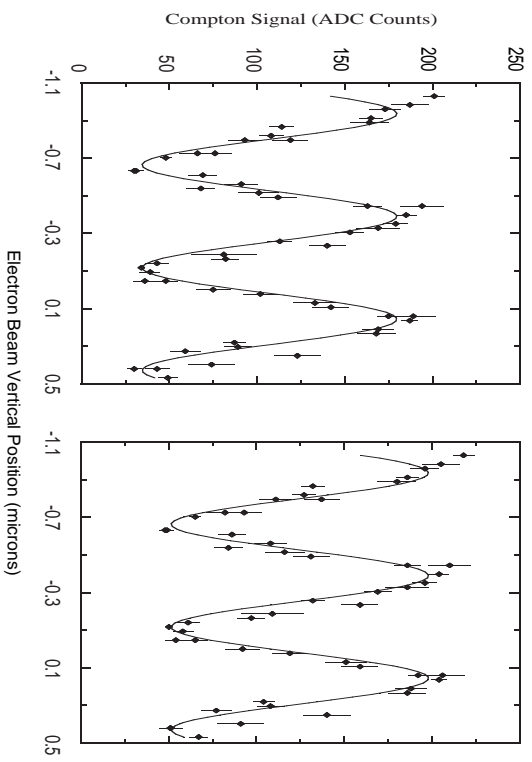


Figure 24: Beam size measurement using  $174^\circ$  mode, both with (left) and without (right) subtraction of background. The decrease in modulation depth due to backgrounds causes the measured spot size to increase from 75 nm to 88 nm.

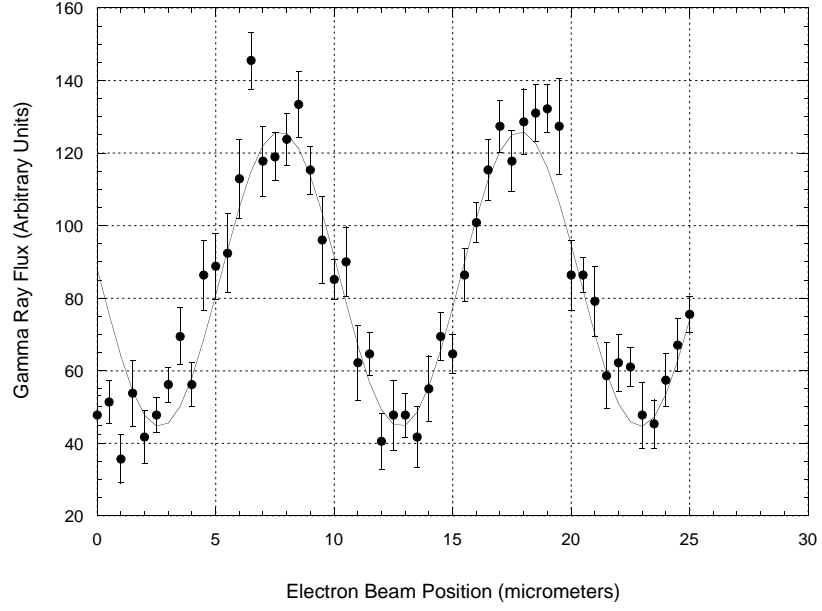


Figure 25: Horizontal beam size measurement made with  $6^\circ$  mode. The measured Compton intensity (points) and sinusoidal fit (solid) are shown. modulation depth is 47.8%, corresponding to a beam size of  $1.95 \mu\text{m}$ .

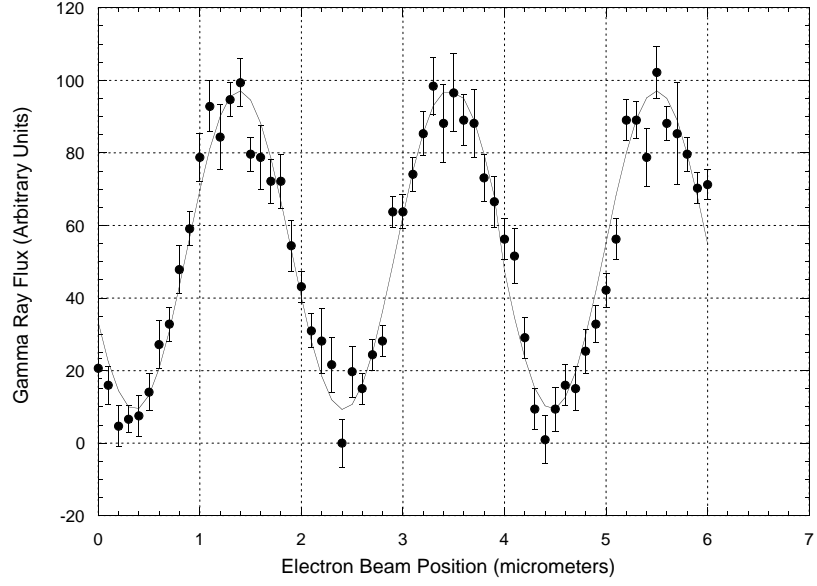


Figure 26: Vertical spot size measured with  $30^\circ$  mode. The modulation depth is 82.6%, corresponding to a beam size of 90 nm.

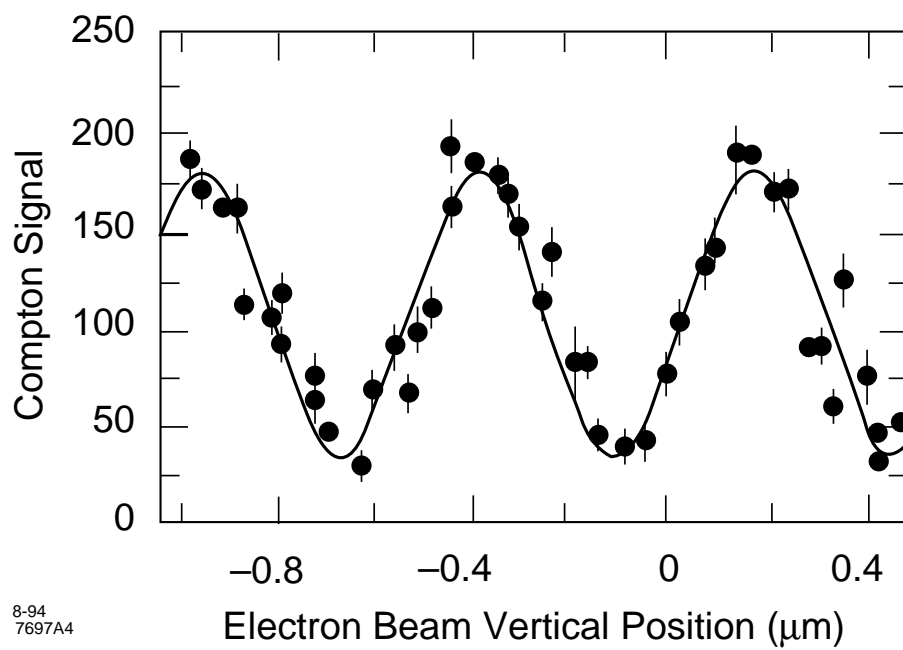


Figure 27: Vertical beam size measured with  $174^\circ$  mode. The modulation depth is 66%, corresponding to a beam size of 77 nm.



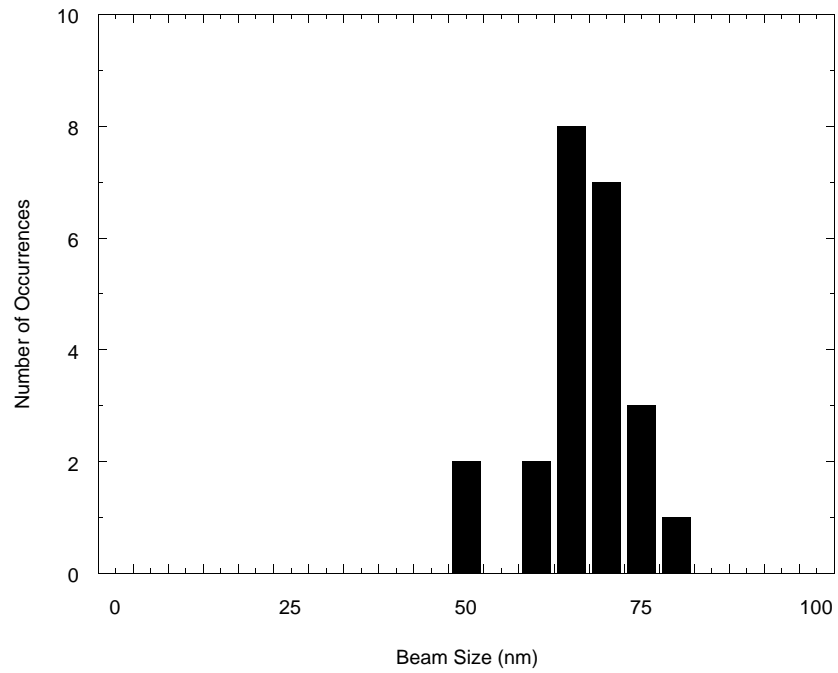


Figure 28: Distribution of 23 measurements made with the FFTB laser-interferometer beam size monitor over a 3 day period in December of 1997.